Nano Research

Open Access

Research Article

Preparation and characterization of a new magnetic fluid with good low temperature resistance

Shilin Nie[1] and Decai Li[1,2] ✉

[1] *Department of Mechanical Engineering, Tsinghua University, Beijing 100084, China*
[2] *State Key Laboratory of Tribology in advanced equipment, Tsinghua University, Beijing 100084, China*

Cite this article: *Nano Research*, **2025**, *18*, 94906997. https://doi.org/10.26599/NR.2025.94906997

ABSTRACT: Magnetic fluids are a type of novel functional material that has emerged over the past two decades, which have found applications in various aspects of production and daily life. However, the application of conventional magnetic fluids in low-temperature environments is severely limited and often unsatisfactory. To address this issue, we have developed a new magnetic fluid with excellent low-temperature resistance. Initially, bare Fe_3O_4 magnetic nanoparticles (FMNPs) were synthesized via co-precipitation without a protective gas. Subsequently, these particles were modified using polyethylene glycol (PEG)-4000 as a surfactant. The bare and modified FMNPs (MFMNPs) were characterized using X-ray diffraction (XRD), vibrating sample magnetometer (VSM), transmission electron microscopy (TEM), Fourier transform infrared spectroscopy (FTIR), and thermogravimetric analysis-differential thermal gravimetric (TGA-DTG) analysis. The rheological properties, low-temperature resistance of the magnetic fluid were also evaluated. The characterization results indicate that the MFMNPs are spherical and monodisperse, with a narrow size distribution and a mean particle size of approximately 12 nm. Furthermore, the FTIR spectra and TGA-DTA results suggest that PEG-4000 is linked to the bare Fe_3O_4 particles via hydrogen bonding, indicating successful modification of the Fe_3O_4 magnetic nanoparticles using PEG. VSM measurements demonstrate that surface modification does not alter the crystal morphology or superparamagnetic of Fe_3O_4. However, it does reduce the saturation magnetization from 68.17 to 54.75 emu/g. Additionally, the prepared magnetic fluid exhibits shear thinning and magnetic viscosity effects. It also exhibits excellent low-temperature resistance, maintaining good fluidity without freezing even at –60 °C. In summary, these results collectively indicate that the new low-temperature resistant magnetic fluid developed in this study is stable and has broad application prospects.

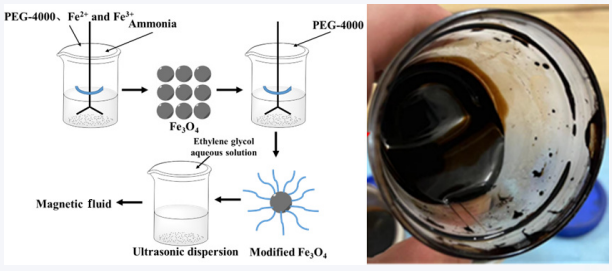

KEYWORDS: magnetic fluid, low-temperature resistance, polyethylene glycol, ethylene glycol aqueous solution, superparamagnetic

1 Introduction

Magnetic fluids, a cutting-edge material in smart functional materials, have found widespread applications in various high-tech fields, including aerospace [1–5], electronic technology [6, 7], machinery [8–11], chemical engineering [12], energy metallurgy [13–15], optics [16–19], biomedicine [20–26], and more [27, 28]. Generally, magnetic fluids are a type of colloidal liquid composed of nano-scale magnetic particles that are highly dispersed in a base carrier liquid (usually organic solvent or water). The interaction between the base carrier liquid and the nano-magnetic particles gives magnetic fluids their unique properties, combining solid magnetic properties with fluid properties. To prevent magnetic particles from agglomerating due to gravity, inter-particle magnetic forces, and van der Waals forces, each nanoparticle requires a surfactant coating [29–31].

In the field of magnetic fluid preparation technology, ester-based [32–34], kerosene-based [35, 36], silicon oil-based [37], and water-based [38–42] magnetic fluids have been relatively well-developed. However, these magnetic fluids often exhibit excessive viscosity or solidification at low temperatures, limiting their applications. In recent years, perfluoropolyether oil-based magnetic fluids have shown superior performance at low temperatures [29–31]. For instance, research conducted by Hongchao Cui and Decai Li has demonstrated that perfluoropolyether oil-based magnetic fluids exhibit low average volatile rates and can operate between –40 and

Received: June 15, 2024; **Revised:** August 10, 2024
Accepted: August 12, 2024

✉Address correspondence to lidecai@mail.tsinghua.edu.cn

200 °C without undergoing oxidation or decomposition [30]. Additionally, Liu Hanyong and his colleagues found that this type of magnetic fluid maintains fluidity even at −70 °C [43]. Nevertheless, perfluoropolyether oil is expensive and not easily accessible. Moreover, only specific perfluoropolyether surfactants can effectively disperse nanoparticles in perfluoropolyether oil, which exhibits limited solubility at room temperature, posing challenges for certain room temperature applications [44]. Therefore, there is a pressing need for a magnetic fluid that offers stable performance at low temperatures with cost-effective and easily accessible.

The excellent low-temperature resistance of magnetic fluids implies that they possess a relatively low freezing point. From the composition of magnetic fluids, it can be seen that the magnetic particles are solid and are not affected by low temperatures. The surfactants adhere to the surface of the magnetic particles in a small amount, and their impact can be ignored. Therefore, the freezing point of magnetic fluids is mainly determined by the base carrier liquid with the largest ratio. After a literature review and analysis [29–31, 43, 44], we identified ethylene glycol (EG) aqueous solution as a suitable base carrier solution [45]. Ethylene glycol is a colorless, slightly viscous liquid with a boiling point of 197.4 °C and a freezing point of −11.5 °C. It can be mixed with water (W) in any proportion. When mixed, the vapor pressure of the water can be altered, significantly reducing its freezing point. Within a certain range, the freezing point of the mixed solution gradually decreases with an increase in ethylene glycol content; when the ethylene glycol content is 68%, the freezing point of the mixed solution can be reduced to −68 °C [46]. Therefore, this study provides a method for preparing a low-temperature-resistant ethylene glycol aqueous solution-based magnetic fluid. The low-temperature-resistant magnetic fluid prepared by this method exhibits excellent low-temperature resistance, maintaining good fluidity without freezing at −60 °C.

2 Results and discussion

2.1 X-ray diffraction (XRD)

The saturation magnetization of magnetic fluids is a crucial metric for evaluating their performance. This metric is primarily determined by the magnetic particles present in the fluid. Consequently, to achieve magnetic fluids with a high saturation magnetization, the preparation of magnetic particles is of utmost importance.

In this paper, the magnetic particles are Fe_3O_4 particles prepared by chemical co precipitation method, the reaction equation is as follows [1, 2]

$$2Fe^{3+} + Fe^{2+} + 8OH^- \rightarrow Fe_3O_4 + 2H_2O$$

This reaction produces nanoscale Fe_3O_4 magnetic particles by co precipitation of Fe^{3+} and Fe^{2+} under alkaline conditions. In order to obtain Fe_3O_4 particles with the highest saturation magnetization, we investigated the affection of reaction temperature on Fe_3O_4 magnetic particles.

In the conducted experiment, where all other parameters remained consistent, Fe_3O_4 magnetic particles were synthesized at various water bath temperatures, specifically at 35, 45, 55, 65, 75, and 85 °C. Subsequently, the prepared magnetic particles underwent XRD characterization. The outcomes of this characterization are presented as follows.

The XRD patterns depicting the Fe_3O_4 magnetic nanoparticles (FMNPs) synthesized at varying temperatures, alongside the modified FMNPs (MFMNPs), are illustrated in Fig. 1. Notably, characteristic diffraction peaks emerge consistently across all temperature-prepared magnetic particles at 2θ values of 30.01°, 35.41°, 43.11°, 53.61°, 56.91°, and 62.41°. These peaks correspond to the (220), (311), (400), (422), (511), and (440) lattice planes of the Fe_3O_4 standard card (JCPDS 88-0315), respectively, with no observable impurity peaks [31]. This finding unequivocally confirms that the synthesized magnetic particles are solely composed of Fe_3O_4. Furthermore, utilizing the Scherrer formula, the average particle sizes of the FMNPs and MFMNPs were determined to be 14.5 and 12 nm, respectively. Remarkably, the XRD pattern of the MFMNPs closely mirrors that of the FMNPs, indicating that the modification process does not alter the inverse spinel structure of the Fe_3O_4 crystal phase. The broadened peaks observed in the XRD pattern of the MFMNPs, attributed to grain refinement [47], suggest that PEG-4000 has been successfully coated onto the FMNPs, thereby restricting the uninterrupted growth of Fe_3O_4 crystals.

2.2 Vibrating sample magnetometer (VSM)

Figure 2 illustrates the magnetic characteristics of Fe_3O_4 particles synthesized at various temperatures, emphasizing the correlation between the saturation magnetization of these particles and the preparation temperature. Evidently, both magnetization curves exhibit an "S" shape, devoid of hysteresis, remanence, or coercivity, signifying that the modification process does not compromise the superparamagnetic properties. Notably, the saturation magnetization of the magnetic particles exhibited an initial increase followed by a decrease as the preparation temperature rose. The

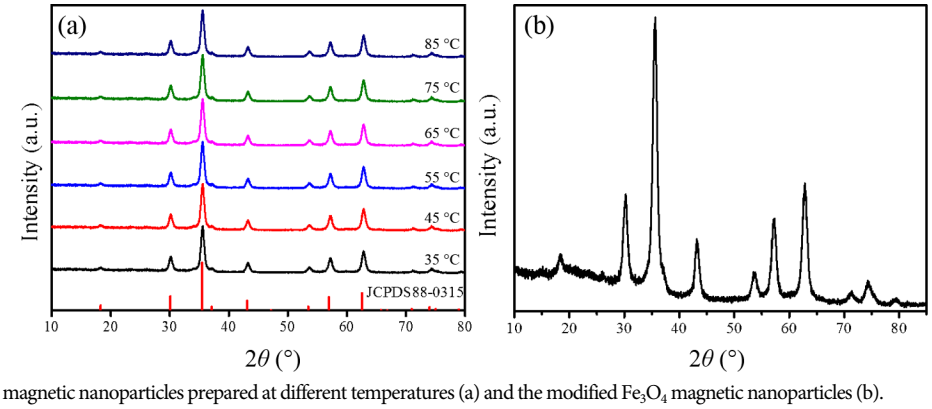

Figure 1 XRD of Fe_3O_4 magnetic nanoparticles prepared at different temperatures (a) and the modified Fe_3O_4 magnetic nanoparticles (b).

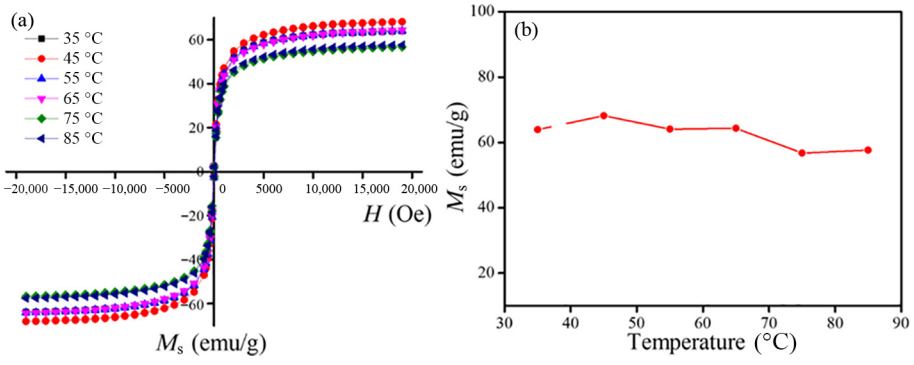

Figure 2 The magnetization curve of Fe_3O_4 particles prepared at different temperatures (a) and the relationship between saturation magnetization of magnetic particles and preparation temperature (b).

optimal saturation magnetization of the magnetic particles, measured at 68.17 emu/g, was achieved at a temperature of 45 °C. XRD analysis revealed no substantial variations in the particle size across the different preparation temperatures. Consequently, to produce magnetic liquids with enhanced saturation magnetization, 45 °C is determined to be the most favorable temperature for the preparation of magnetic particles.

The magnetic properties of both FMNPs and MFMNPS were meticulously measured using VSM at a temperature of 300 K, as presented in Fig. 3. Akin to the observations in Fig. 2, the magnetization curves pertaining to MFMNPs exhibit an "S" shape, absent of hysteresis, remanence, or coercivity. This finding underscores that the modification process does not perturb the superparamagnetic behavior. However, a notable reduction in saturation magnetization (M_s) was observed post-modification, with a decrease from 68.17 to 54.75 emu/g. This decrease can be attributed to three primary factors: Firstly, the incorporation of PEG-4000, a non-magnetic material, inherently leads to a decrease in magnetization per unit mass. Secondly, the coating process introduces random spin, which subsequently diminishes magnetic orientation and weakens the inter-particle interactions. This phenomenon has been previously documented with other surfactants [48]. Lastly, it is worth mentioning that M_s is directly proportional to particle size [49], and the PEG-4000 coating facilitates the production of smaller particles, thus contributing to the observed reduction in saturation magnetization.

2.3 Transmission electron microscopy (TEM)

To gain a deeper understanding of the surface morphology and particle size distribution characteristics of FMNPs and MFMNPs, TEM analysis was conducted. The resulting TEM images and particle size distributions for both FMNPs and MFMNPs are presented in Fig. 4. Upon examination of the TEM images (specifically Figs. 4(d)–4(f)), it becomes evident that the FMNPs possess a smaller particle size with a more uniform distribution. The particle size of the FMNPs ranges between 10 and 30 nm, with an average particle size of approximately 14.9 nm (as indicated in the inset of Fig. 4(f)). This finding aligns closely with the particle size estimations obtained via XRD analysis. However, it is worth noting that there is some degree of aggregation present, with a majority of the magnetic particles clustering together to form larger secondary particles. In contrast, the MFMNPs exhibit a notably small particle size, uniform distribution, and excellent dispersibility. Their particle size falls within the range of 5–20 nm, boasting an average particle size of only 12 nm (as shown in the inset of Fig. 4(c)). The MFMNPs are observed to be homogenously dispersed,

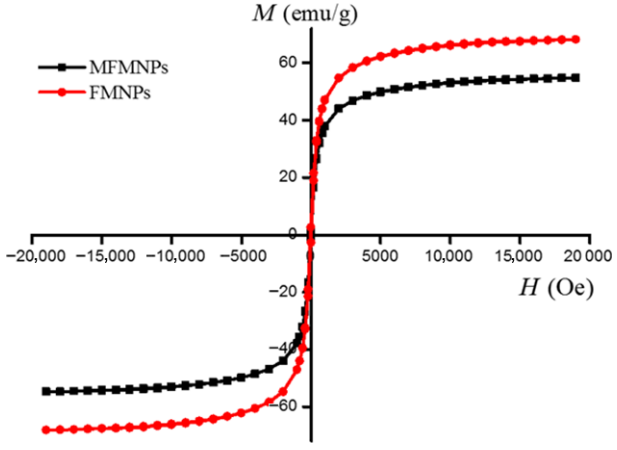

Figure 3 The magnetization curve of FMNPs and MFMNPs.

lacking any signs of flocculation. They are predominantly spherical in shape with well-defined boundaries, as demonstrated in Figs. 4(a)–4(c). These observations strongly suggest that the utilization of PEG-4000 has significantly improved the dispersibility of Fe_3O_4 and led to a considerable reduction in particle size. This, in turn, enhances the feasibility of obtaining stable magnetic fluids, owing to the optimized physical characteristics imparted by the PEG-4000 coating.

The morphological disparities observed between FMNPs and MFMNPs can be attributed to the influence of PEG-4000, which serves a dual purpose. Firstly, PEG-4000 firmly adsorbs onto the surface, thereby impeding crystal growth. Secondly, its long chain introduces steric hindrance, effectively mitigating particle agglomeration. As a result, the PEG-4000 layer plays a pivotal role in restricting the expansion of FMNPs while enhancing their dispersion.

2.4 Fourier transform infrared spectroscopy (FT-IR)

The FT-IR spectra depicted in Fig. 5, showcasing FMNPs, MF MNPs, and pure PEG-4000, reveal that the absorption peaks predominantly reside within the fingerprint region. Upon spectral analysis, it was found that the FMNPs exhibited a broad and intense absorption peak near 3400 cm^{-1} and an absorption peak near 1620 cm^{-1}, which are characteristic absorption peaks of hydroxyl groups, indicating the presence of a large number of hydroxyl groups on the surface of the FMNPs. After modification, the hydroxyl absorption peaks near 3400 and 1600 cm^{-1} disappeared, indicating that PEG-4000 is adsorbed on the surface of the magnetic particles through hydrogen bonding, which is a state

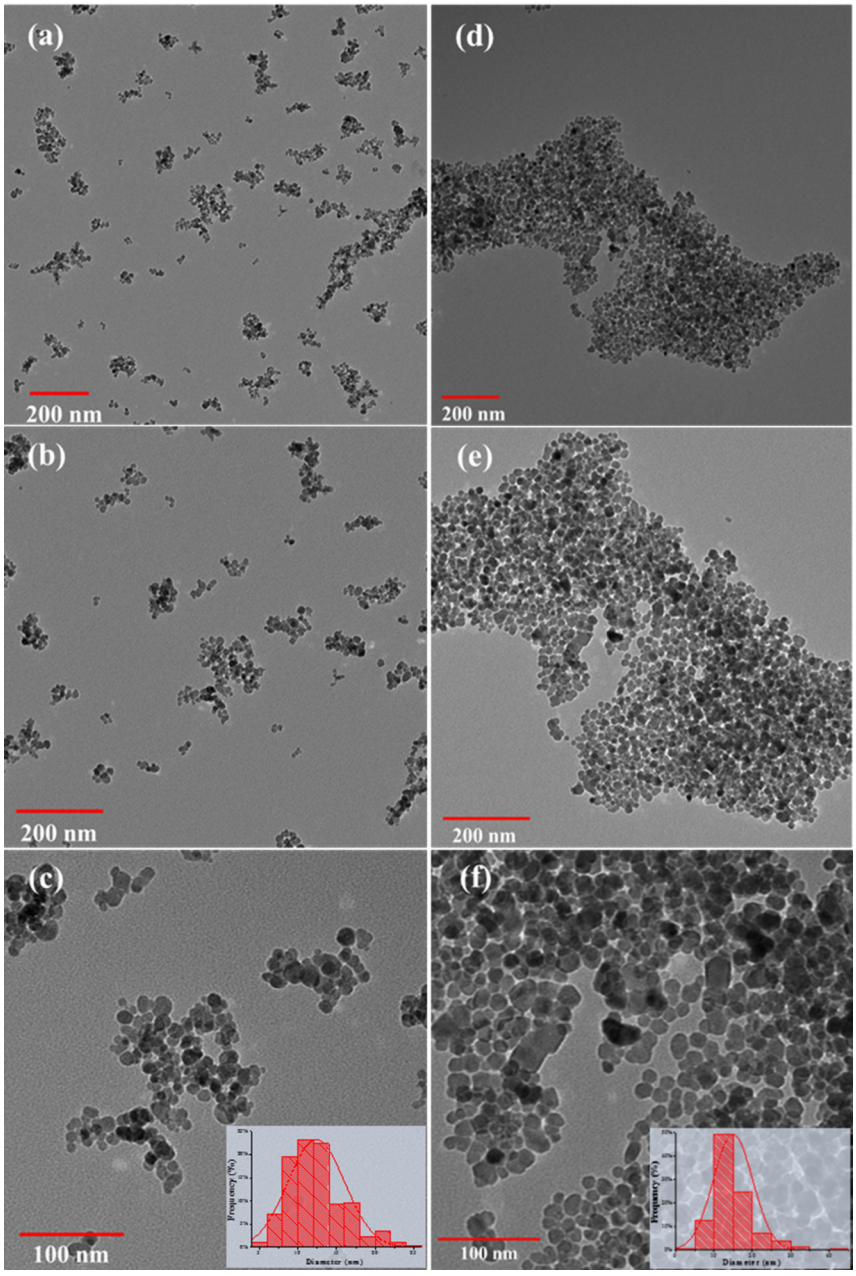

Figure 4 TEM and particle size distribution of FMNPs and MFMNPs. (a)–(c) MFMNPs; (d)–(f) FMNPs; particle size distribution: inset.

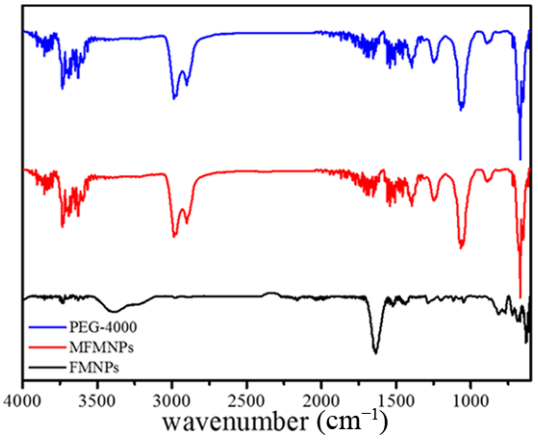

Figure 5 FT-IR spectra of FMNPs, MFMNPs, and pure PEG-4000.

of physical adsorption. At the same time, the appearance of absorption peaks near 2900 and 2800 cm^{-1} indicated the presence of $-CH_3$ and $-CH_2-$, and the characteristic absorption peaks near 1250 and 1055 cm^{-1} indicated the presence of –C–O–C–; pure PEG-4000 also exhibited characteristic absorption peaks for $-CH_3$ and $-CH_2-$ near 2900 and 2800 cm^{-1}, as well as absorption peaks for –C–O–C– near 1250 and 1055 cm^{-1}. These results indicate that PEG-4000 was successfully adsorbed on the surface of the particles, indicating successful modification.

2.5 Radial distribution function (RDF)

In order to better explain the interaction between PEG-4000 and Fe_3O_4, a molecular dynamics model was established and analyzed by materials studio. As illustrated in the figures, the initial steps involved the individual construction of the Fe_3O_4 unit cell (Fig. 6(b)) and the PEG-4000 molecular model (Fig. 6(a)). Subsequently,

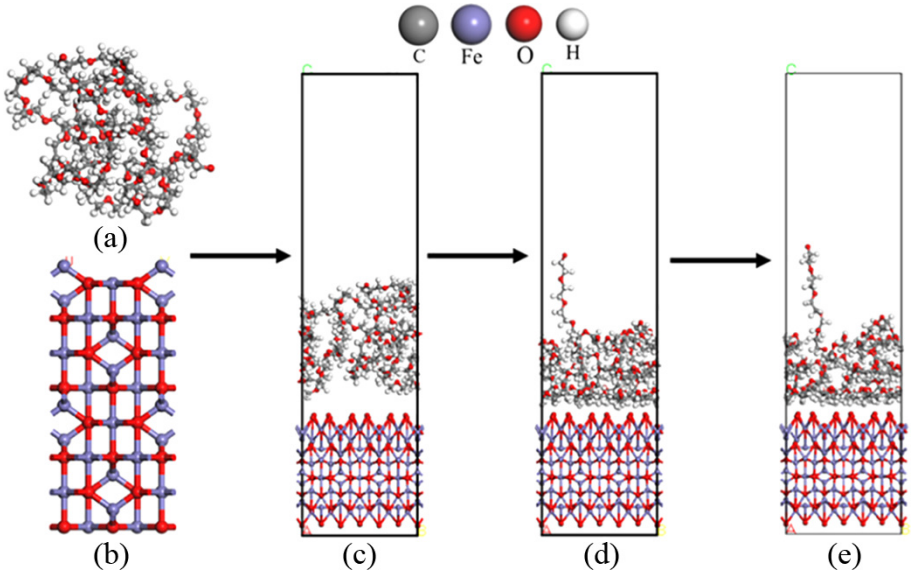

Figure 6 Molecular dynamics model of PEG-4000 and Fe_3O_4. (a) PEG-4000; (b) Fe_3O_4; (c) adsorption model of PEG-4000 and Fe_3O_4; (d) geometric optimized adsorption model; (e) adsorption model after molecular dynamics simulation.

the amorphous cell module was leveraged to construct and refine the adsorption model of PEG-4000 molecules onto the Fe_3O_4 unit cell (Figs. 6(c) and 6(d)).

After that, the Forcite module within the software was employed for molecular dynamics simulations. The COMPASS II force field was selected to describe the interactions. The van der Waals and electrostatic interactions were accurately computed using the Ewald method, with a time step of 1 fs. The simulations were conducted under NVE ensemble conditions at 355 K for a duration of 500 ps (Fig. 6(e)) [50, 51].

To quantify the interactions between the two components, the RDF was utilized [50–53]. RDF represents the probability of finding an atom at a specific distance from another atom, relative to a random distribution. By analyzing the RDF, $g(r)$, between H and O atoms, the nature of interactions could be discerned based on the peak positions, corresponding to hydrogen bonding [1.8 Å < $g(r)$ < 3.1 Å], strong van der Waals forces [3.1 Å < $g(r)$ < 5 Å], and weak van der Waals forces [$g(r)$ > 5 Å] [54]. The RDF plot for H–O atoms is presented in the accompanying Fig. 7.

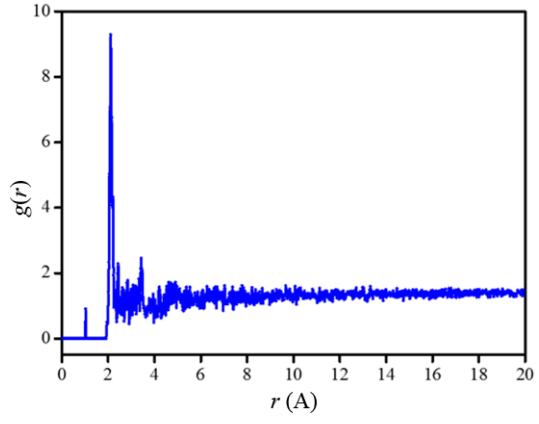

Figure 7 RDF between O and H atoms.

The RDF O–H curve exhibits a prominent peak near 0.25 nm, with a maximum value of approximately 10, indicating the presence of hydrogen bonds between Fe_3O_4 and PEG-4000 [50, 54]. This finding confirms that PEG-4000 molecules are adsorbed onto the surface of Fe_3O_4 nanoparticles through hydrogen bonding, which is consistent with infrared spectroscopic results.

2.6 TG-DTG

The TG-DTG results for FMNPs and MFMNPs, as presented in Fig. 8, reveal distinct weight loss patterns with increasing temperature. These patterns can be segmented into three distinct stages. Initially, a rapid weight loss stage occurs below 100 °C, which can be primarily attributed to the desorption of water molecules adsorbed on the surfaces of both FMNPs and MFMNPs. The high surface area and abundance of hydrophilic hydroxyl groups on these nanoparticles facilitate significant water adsorption from the ambient air. In the second stage, spanning from 100 to 300 °C, the nanoparticles exhibit an initial weight increase followed by a decrease. This behavior is associated with the transformation of Fe_3O_4 to Fe_2O_3 upon exposure to an oxygen-rich environment at elevated temperatures. However, it is noteworthy that the rate of weight increase for MFMNPs is markedly lower than that observed for FMNPs. This difference can be attributed to the presence of surfactant PEG-4000 adsorbed on the surface of MFMNPs, which also undergoes weight loss at these elevated temperatures. The third stage is characterized by a constant weight observed above 300 °C. This stability is due to the formation of Fe_2O_3, which remains relatively unchanged at these high temperatures. Furthermore, it is observed that the final residual mass of MFMNPs is significantly lower than that of FMNPs. This finding provides additional evidence for the successful modification of Fe_3O_4 magnetic particles with the surfactant PEG-4000. The combination of these factors results in distinct thermal properties and weight loss patterns for the modified MFMNPs compared to the unmodified FMNPs.

2.7 Viscosity curves

In the experiment, the viscosity curves of low-temperature resistant magnetic fluids with different base carrier ratios were measured under different external magnetic fields. As observed in Fig. 9, it can be seen that the viscosity of all magnetic fluid samples decreases to a stable value with the increase of shear rate, under different magnetic field intensities. Additionally, the decay rate also gradually

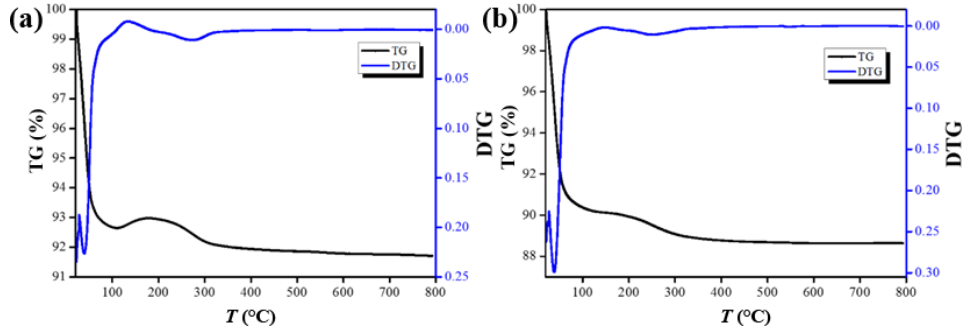

Figure 8 TG-DTG of (a) FMNPs and (b) MFMNPs.

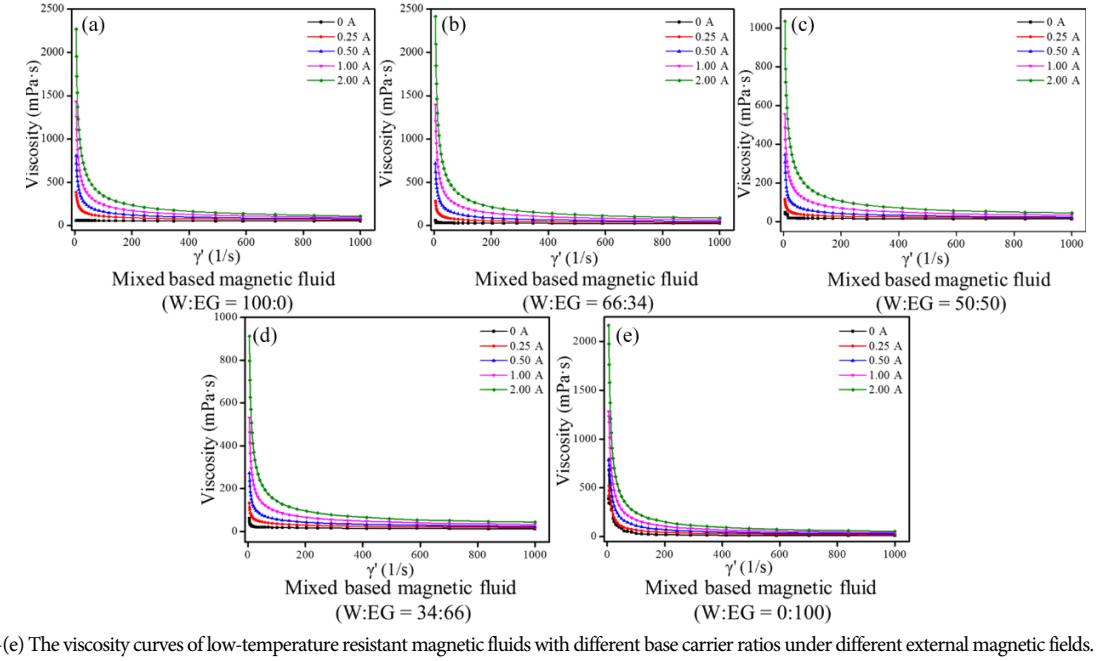

Figure 9 (a)–(e) The viscosity curves of low-temperature resistant magnetic fluids with different base carrier ratios under different external magnetic fields.

decreases. This indicates that all magnetic fluid samples exhibit the shear thinning phenomenon. Moreover, it is observed that for the same magnetic fluid sample, viscosity increases as the external magnetic field increases. This occurs because the magnetic particles in magnetic fluids agglomerate under the influence of the external magnetic field, forming chain or network structures. These structures increase the yield stress of the magnetic fluid, leading to greater flow obstruction. On a macro level, this manifests as an increase in the viscosity of the magnetic fluid [55]. According to the model of dipole chains subjected to stretching [56], the yield stress of magnetic fluids can be calculated as follows

$$\tau_s = n_t \frac{3\mu_0}{\pi r^4} m_d^2$$

where n_t represents the number of chains per unit area; μ_0 represents vacuum permeability; r represents the average radius of solid particles; m_d represents the average magnetic moment of solid particles.

Therefore, the formation of chain structures in magnetic fluids leads to a direct correlation between their yield stress and flow obstruction. Specifically, the longer the chain length and the greater the angle between the chain direction and the flow direction of the magnetic fluids, the more significant the obstructive effect on fluid flow, resulting in an elevation of the magnetic fluid's viscosity. As the intensity of the magnetic field increases, the chain structure gradually grows and elongates, further enhancing the viscosity of the fluid. Consequently, the viscosity of the magnetic fluid gradually rises under the influence of the magnetic field [55].

Figure 9 also shows the variation of viscosity of magnetic liquid with shear rate, which can be attributed to shear thinning. The shear force on magnetic liquids follows Newton's law

$$\tau = \eta \frac{\partial \mu}{\partial y} = \eta D$$

As the shear rate D increases, the shear stress τ also rises. When subjected to a magnetic field, the magnetic fluid experiences shear forces, which result in the longer chains of dipoles breaking down into shorter ones. The higher the shear rate, the more extensive the destruction of the chain structure within the magnetic fluid becomes. Consequently, the smaller the size of the disrupted microstructures, the less obstruction they pose to the fluid's flow, leading to a decrease in the macroscopic viscosity of the magnetic fluid. Once the shear rate reaches a certain threshold, the aggregated structures within the magnetic fluid are largely destroyed, and the magnetic particles become uniformly dispersed. At this point, the viscosity remains relatively constant, unaffected by further increases in the shear rate [55].

2.8 The performance of low temperature resistance

The exceptional low-temperature resistance exhibited by magnetic

fluids underscores their possession of a notably low freezing point, rendering them ideally suited for diverse applications within cold environments. The determination of this freezing point typically involves a range of experimental techniques, including but not limited to the experimental method [57], the thermistor temperature-testing method [58, 59], electrical potential measurement [60], electrical resistance measurement [61], differential scanning calorimetry [62], pulsed nuclear magnetic resonance [63], and the frequency domain reflection method [64]. In this study, the choice of experimental methodology was guided by considerations of both simplicity in execution and clarity of outcomes, leading to the adoption of a straightforward yet effective approach for assessing the freezing point of magnetic liquids. This methodology provides a reliable means to investigate the low-temperature behavior of these fluids, with implications for their utilization in various cold-environment applications.

To assess the low-temperature resilience of magnetic fluids, we conducted a series of tests using chambers capable of simulating high and low temperatures. Six samples of magnetic fluid with varying base carrier ratios were placed in the chamber and exposed to –60 °C for a duration of 2 h, as shown in Fig. 10. Following this exposure, we observed their flow characteristics. The results indicated that the magnetic fluid exhibiting the most robust low-temperature performance occurred when the ratio of water to ethylene glycol was maintained at 34:66. Notably, even after being maintained at –60 °C for 2 h, this fluid retained its liquid state and exhibited impressive fluidity. This exceptional low-temperature tolerance suggests that this particular ratio of magnetic fluid is highly suitable for use in specific low-temperature environments.

The optimal ratio of water to ethylene glycol enhances the low-temperature tolerance of magnetic fluids. By blending ethylene glycol with water, an aqueous solution that modifies the vapor pressure of both components is formed. Consequently, this solution exhibits a significantly lower freezing point compared to pure water or ethylene glycol alone. The detailed analysis is as follows:

According to the colligative property of dilute solutions [65], the dissolution of non-volatile substances (ethylene glycol) in solvents (water) can lead to a lower freezing point of the formed solution:

At a constant pressure, the freezing point of the solvent in the solution is T_f.

When solid–liquid two-phase equilibrium coexists, the solid phase chemical potential is equal to the liquid phase chemical potential [65, 66]

$$\mu_{A(l)}(T,P,x_A) = \mu_{A(s)}(T,P)$$

At a temperature of $T + dT$

$$\mu_{A(l)} + d\mu_{A(l)} = \mu_{A(s)} + d\mu_{A(s)}$$

$$\mu_{A(l)} = \mu_{A(s)} \qquad d\mu_{A(l)} = d\mu_{A(s)}$$

$$\left(\frac{\partial \mu_{A(l)}}{\partial T}\right)_{p,x_A} dT + \left(\frac{\partial \mu_{A(l)}}{\partial x_A}\right)_{T,p} dx_A = \left(\frac{\partial \mu_{A(s)}}{\partial T}\right)_p dT$$

For dilute solutions [65] $\mu_A = \mu_A^\star + RT\ln x_A$

And also known $\left(\frac{\partial \mu_{A(l)}}{\partial T}\right)_{p,n_B,n_C} = -S_B$

Obtain $-S_{A(l)}dT + \frac{RT}{x_A}dx_A = -S^\star_{m,A(s)}dT$

And because

$$S_{A(l)} - S^\star_{m,A(s)} = \frac{H_{A(l)} - H^\star_{m,A(s)}}{T} = \frac{\Delta H_{m,A}}{T}$$

For dilute solutions, set $\Delta H_{m,A} \approx \Delta_{fus}H^\star_{m,A}$

So can get $\frac{RT}{x_A}dx_A = \frac{\Delta_{fus}H^\star_{m,A}}{T}dT$

Integral over equation $\oint_1^{x_A}\frac{dx_A}{x_A} = \int_{T_f^*}^{T_f}\frac{\Delta_{fus}H^\star_{m,A}}{RT^2}dT$

Set the $\Delta_{fus}H^\star_{m,A}$ is temperature independent [61, 62]

$$\ln x_A = \frac{\Delta_{fus}H^\star_{m,A}}{R}\left(\frac{1}{T_f^\star} - \frac{1}{T_f}\right) = \frac{\Delta_{fus}H^\star_{m,A}}{R}\left(\frac{T_f - T_f^\star}{T_f T_f^\star}\right)$$

If instructed $\Delta T_f = T_f^\star - T_f$, $T_f T_f^\star \approx (T_f^\star)^2$

There are

$$-\ln x_A = \frac{\Delta_{fus}H^\star_{m,A}}{R(T_f^\star)^2}\cdot\Delta T_f$$

Expand the series, assuming $\ln(1-x) = -x$

$$-\ln x_A = \ln(1-x_B) \approx x_B \approx \frac{n_B}{n_A}$$

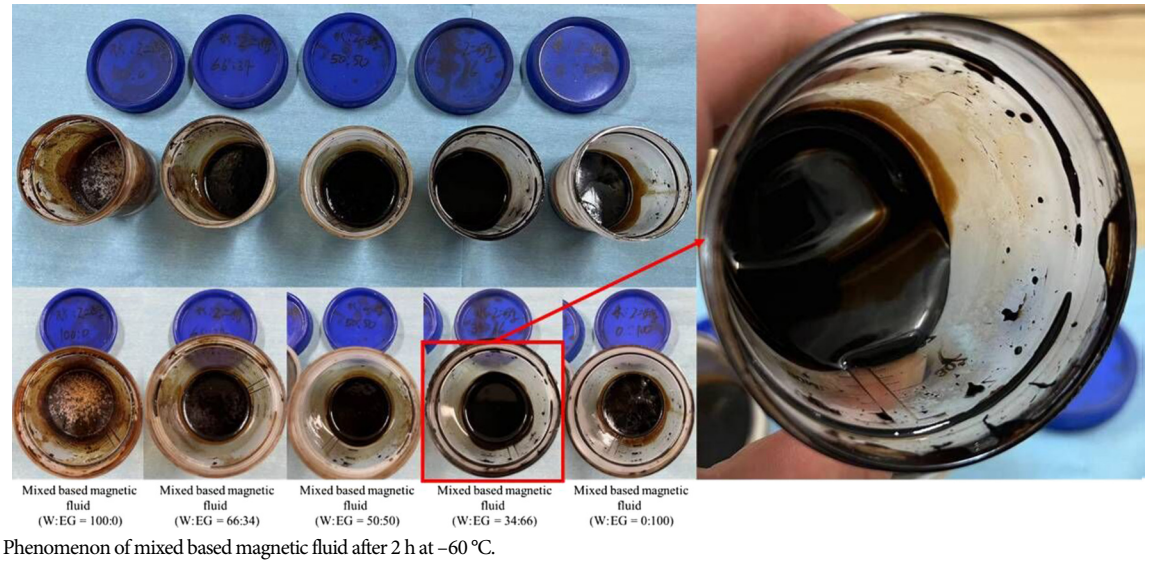

Figure 10 Phenomenon of mixed based magnetic fluid after 2 h at –60 °C.

Bring into the equation above

$$\Delta T_f = \frac{R(T_f^*)^2}{\Delta_{fus}H^*_{m,A}} \cdot \frac{n_B}{n_A}$$

Have

$$\Delta T_f = \frac{R(T_f^*)^2}{\Delta_{fus}H^*_{m,A}} \cdot M_A \left(\frac{m(B)}{M_B m(A)}\right) = k_f \left(\frac{m(B)}{M_B m(A)}\right)$$

$$\Delta T_f = k_f m_B$$

Inside the formula, $k_f = \frac{R(T_f^*)^2}{\Delta_{fus}H^*_{m,A}} M_A$ is freezing reduction constant, unit is K·kg/mol; it is related to the properties of solvents, and the freezing reduction constant of common solvents can be found in the table.

Convert the ratio of ethylene glycol to water in the prepared low-temperature resistant mixed magnetic fluid-based carrier to the molar mass of ethylene glycol:

When the ratio of water to ethylene glycol is 34:66, $m_{(\text{ethylene glycol})}$ = 34.8 mol/kg.

Look up the book, it can be found that the freezing reduction constant of water, k_f = 1.86 K·kg/mol.

It can be calculated by introducing the freezing point reduction formula

$$\Delta T_f = 64.73\ \text{K}$$

When the ratio of water to ethylene glycol is 34:66, the freezing point of the ethylene glycol aqueous solution decreases to −64.73 °C, which is consistent with the results of low-temperature testing.

3 Conclusions

In summary, a low-temperature magnetic fluid was successfully prepared by dispersing PEG-4000-modified magnetic nanoparticles in a mixture of ethylene glycol and water, varying the solvent ratios. These magnetic nanoparticles were meticulously fabricated using the chemical co-precipitation method. Characterization via XRD, VSM, and TEM confirmed an optimal preparation temperature of 45 °C, resulting in magnetic particles exhibiting a high saturation magnetization of 68.17 emu/g, a nanoscopic size of 14 nm, and excellent dispersion, essential for magnetic fluid applications. FT-IR and TG analysis further revealed that the PEG-4000 surfactant effectively modified the magnetic particles, leading to smaller, more uniformly distributed particles averaging 12 nm in size. The magnetic fluid prepared using this method exhibited remarkable stability. A low-temperature resistance test demonstrated that a 66:34 ratio of ethylene glycol to water yielded the most resilient magnetic fluid. Following exposure to −60 °C for 2 h, the fluid maintained its liquid state, exhibiting excellent fluidity. This innovative low-temperature resistant magnetic fluid holds promising applications across multiple industries.

4 Experimental

4.1 Chemicals and reagents

Unless specified, all chemicals were directly used without purification. Ferric chloride ($FeCl_3$) is purchased from Shanghai Titan Scientific Co., Ltd. Iron chloride tetrahydrate ($FeCl_2{\cdot}4H_2O$) was procured from Tianjin Damao Chemical Industry Group Co., Ltd. Ammonium hydroxide (25%) was procured from Xilong Scientific Co., Ltd. Ethylene glycol was purchased from Beijing Chemical Industry Group Co., Ltd. PEG-4000 was obtained from Shanghai Yien Chemical Technology Co., Ltd. Water used in all experiment processes was deionized water, which was refined and filtered by an ultrapure water machine (PSDK2-20-C) in the lab.

4.2 Preparation and characterization

To prepare the magnetic fluid which can satisfy low temperature demands in applications, Fe_3O_4 magnetic nanoparticles were synthesized by co-precipitation without protective gas [1]. Then the Fe_3O_4 magnetic nanoparticles were modified by polyethylene glycol-4000 surfactant. After modification, the Fe_3O_4 magnetic nanoparticle was dispersed in mixed solution of water and ethylene glycol by ultrasonic. Water-ethylene glycol mixed solution-based magnetic fluid was obtained after 2 to 3 h of ultrasonic.

Morphology and composition of the as-synthesized samples were characterized by XRD (Rigaku D/Max 2500H), TEM (Hitachi HT7700), and FT-IR (Varian 3100), respectively. The thermal behavior of the as-synthesized samples was tested by thermogravimetry/differential scanning calorimeter (TGA, TA instruments Q5000IR). Magnetic property carried out by VSM (Lakeshore 7307) applied magnetic field was from −10,000 to 10,000 Oe. The low-temperature fluidity of magnetic fluids were tested by placing them in a low temperature (−60 °C) for 2 h. The viscosity tested of mixed solution-based magnetic fluid was at shear rate $D = 3.84n\ (1/S)$ at −20 °C in B system by NXE-1B cone-plate viscometer (Anton Paar MCR301) [2].

Data availability

The data underlying this article are available in the article.

Acknowledgements

This research is supported by the National Natural Science Foundation of China (Nos. 51735006, 51927810, and U1837206) and the National Key R&D Program of China (No. 2020YFB2006900).

Declaration of competing interest

There are no conflicts to declare.

Author contribution statement

S. L. N.: Conceptualization, formal analysis, investigation, methodology, validation, visualization, writing – original draft, writing – review & editing. D. C. L.: Conceptualization, funding acquisition, projectadministration, and supervision.

Use of AI statement

None.

References

[1] Li, D. C. Theory and Application of Magnetic Liquids; Science Press: Beijing, 2003.
[2] Li, D. C. Theory and Application of Magnetic Fluid Sealing; Science Press: Beijing, 2010.

[3] Torres-Díaz, I.; Rinaldi, C. Recent progress in ferrofluids research: Novel applications of magnetically controllable and tunable fluids. *Soft Matter* **2014**, *10*, 8584–8602.
[4] Raj, K.; Moskowitz, B.; Casciari, R. Advances in ferrofluid technology. *J. Magn. Magn. Mater.* **1995**, *149*, 174–180.
[5] Imran, M.; Ansari, A. R.; Shaik, A. H.; Abdulaziz; Hussain, S.; Khan, A.; Chandan, M. R. Ferrofluid synthesis using oleic acid coated Fe_3O_4 nanoparticles dispersed in mineral oil for heat transfer applications. *Mater. Res. Express* **2018**, *5*, 036108.
[6] Varshney, S.; Ohlan, A.; Jain, V. K.; Dutta, V. P.; Dhawan, S. K. Synthesis of ferrofluid based nanoarchitectured polypyrrole composites and its application for electromagnetic shielding. *Mater. Chem. Phys.* **2014**, *143*, 806–813.
[7] Mishra, M.; Singh, A. P.; Singh, B. P.; Singh, V. N.; Dhawan, S. K. Conducting ferrofluid: A high-performance microwave shielding material. *J. Mater. Chem. A* **2014**, *2*, 13159–13168.
[8] Ohara, T. Bearing with magnetic fluid seal. U.S. Patent 9,546,685, January 17, 2017.
[9] Szczech, M.; Horak, W. Numerical simulation and experimental validation of the critical pressure value in ferromagnetic fluid seals. *IEEE Trans. Magn.* **2017**, *53*, 4600605.
[10] Marinică, O.; Susan-Resiga, D.; Bălănean, F.; Vizman, D.; Socoliuc, V.; Vékás, L. Nano-micro composite magnetic fluids: Magnetic and magnetorheological evaluation for rotating seal and vibration damper applications. *J. Magn. Magn. Mater.* **2016**, *406*, 134–143.
[11] Hajalilou, A.; Mazlan, S. A.; Lavvafi, H.; Shameli, K. Field Responsive Fluids as Smart Materials; Springer: Singapore, 2016.
[12] Kopyl, S.; Bystrov, V.; Bdikin, I.; Maiorov, M.; Sousa, A. C. M. Filling carbon nanotubes with magnetic particles. *J. Mater. Chem. C* **2013**, *1*, 2860–2866.
[13] Sheikholeslami, M.; Ganji, D. D. Ferrohydrodynamic and magnetohydrodynamic effects on ferrofluid flow and convective heat transfer. *Energy* **2014**, *75*, 400–410.
[14] Kandelousi, M. S. Effect of spatially variable magnetic field on ferrofluid flow and heat transfer considering constant heat flux boundary condition. *Eur. Phys. J. Plus* **2014**, *129*, 248.
[15] Lajvardi, M.; Moghimi-Rad, J.; Hadi, I.; Gavili, A.; Isfahani, T. D.; Zabihi, F.; Sabbaghzadeh, J. Experimental investigation for enhanced ferrofluid heat transfer under magnetic field effect. *J. Magn. Magn. Mater.* **2010**, *322*, 3508–3513.
[16] Martinez, L.; Cecelja, F.; Rakowski, R. A novel magneto-optic ferrofluid material for sensor applications. *Sens. Actuators A: Phys.* **2005**, *123–124*, 438–443.
[17] Miao, Y. P.; Zhang, K. L.; Liu, B.; Lin, W.; Zhang, H.; Lu, Y.; Yao, J. Q. Ferrofluid-infiltrated microstructured optical fiber long-period grating. *IEEE Photonics Technol. Lett.* **2013**, *25*, 306–309.
[18] Zhao, Y.; Wu, D.; Lv, R. Q. Magnetic field sensor based on photonic crystal fiber taper coated with ferrofluid. *IEEE Photonics Technol. Lett.* **2015**, *27*, 26–29.
[19] Zarandi, A. A.; Alvani, A. A. S.; Salimi, R.; Sameie, H.; Moosakhani, S.; Poelman, D.; Rosei, F. Self-organization of an optomagnetic $CoFe_2O_4$-ZnS nanocomposite: Preparation and characterization. *J. Mater. Chem. C* **2015**, *3*, 3935–3945.
[20] Kim, E. H.; Lee, H. S.; Kwak, B. K.; Kim, B. K. Synthesis of ferrofluid with magnetic nanoparticles by sonochemical method for MRI contrast agent. *J. Magn. Magn. Mater.* **2005**, *289*, 328–330.
[21] Zhang, L. Y.; Gu, H. C.; Wang, X. M. Magnetite ferrofluid with high specific absorption rate for application in hyperthermia. *J. Magn. Magn. Mater.* **2007**, *311*, 228–233.
[22] Ganguly, R.; Gaind, A. P.; Sen, S.; Puri, I. K. Analyzing ferrofluid transport for magnetic drug targeting. *J. Magn. Magn. Mater.* **2005**, *289*, 331–334.
[23] Metelkina, O. N.; Lodge, R. W.; Rudakovskaya, P. G.; Gerasimov, V. M.; Lucas, C. H.; Grebennikov, I. S.; Shchetinin, I. V.; Savchenko, A. G.; Pavlovskaya, G. E.; Rance, G. A. et al. Nanoscale engineering of hybrid magnetite-carbon nanofibre materials for magnetic resonance imaging contrast agents. *J. Mater. Chem. C* **2017**, *5*, 2167–2174.
[24] Odenbach, S. Fluid mechanics aspects of magnetic drug targeting. *Biomed. Tech.* **2015**, *60*, 477–483.
[25] Hensley, D.; Tay, Z. W.; Dhavalikar, R.; Zheng, B.; Goodwill, P.; Rinaldi, C.; Conolly, S. Combining magnetic particle imaging and magnetic fluid hyperthermia in a theranostic platform. *Phys. Med. Biol.* **2017**, *62*, 3483–3500.
[26] Hedayatnasab, Z.; Abnisa, F.; Daud, W. M. A. W. Review on magnetic nanoparticles for magnetic nanofluid hyperthermia application. *Mater. Des.* **2017**, *123*, 174–196.
[27] Xiang, P. J.; Yan, L.; Guo, Y. M.; He, X. H.; Gerada, C.; Chen, I. M. A concentrated-flux-type PM machine with irregular magnets and iron poles. *IEEE/ASME Trans. Mechatron.* **2024**, *29*, 691–702.
[28] Xiang, P. J.; Yan, L.; Xiao, H. Y.; He, X. H.; Du, N. N. Development of a novel radial-flux machine with enhanced torque profile employing quasi-cylindrical PM pattern. *IEEE Trans. Energy Convers.* **2023**, *38*, 2772–2783.
[29] Cui, H. C.; Li, D. C. Fabrication and properties research on a novel perfluoropolyether based ferrofluid. *J. Magn. Magn. Mater.* **2019**, *473*, 341–347.
[30] Cui, H. C.; Li, D. C. Preparation and property research of perfluoropolyether oil-based ferrofluid. *J. Supercond. Nov. Magn.* **2018**, *31*, 3607–3624.
[31] Cui, H. C.; Li, D. C.; Zhang, Z. L. Preparation and characterization of Fe_3O_4 magnetic nanoparticles modified by perfluoropolyether carboxylic acid surfactant. *Mater. Lett.* **2015**, *143*, 38–40.
[32] Arora, M.; Singh, R.; Panda, M. K. Effects of magnetic-field-dependent viscosity at onset of convection in magnetic nanofluids. *J. Eng. Math.* **2016**, *101*, 201–217.
[33] Singh, J.; Bajaj, R. Dean instability in ferrofluids. *Meccanica* **2016**, *51*, 835–847.
[34] Luo, J. H.; Zhang, G.; Xie, N. J.; Wang, T. X.; Gu, Y. R.; Gong, S. H.; Wang, C. L. A magnetic sensor based on a hybrid long-period fiber grating and a magnetic fluid. *IEEE Photonics Technol. Lett.* **2015**, *27*, 998–1001.
[35] Fosa, G.; Bădescu, R.; Călugăru, G.; Bădescu, V. Measuring the transmittivity of light: A tool for testing the quality of magnetic liquids. *Opt. Mater.* **2006**, *28*, 461–465.
[36] Lin, J. F.; Wang, C. H.; Lee, M. Z. Linear birefringence and dichroism measurement in oil-based Fe3O4 magnetic nanoparticles. *J. Magn. Magn. Mater.* **2013**, *332*, 192–198.
[37] Zhang, L.; Huang, Z.; Shao, H. P.; Li, Y.; Zheng, H. Effects of γ-Fe_2O_3 on γ-Fe_2O_3/Fe_3O_4 composite magnetic fluid by low-temperature low-vacuum oxidation method. *Mater. Des.* **2016**, *105*, 234–239.
[38] Guo, T. X.; Bian, X. F.; Yang, C. C. A new method to prepare water based Fe_3O_4 ferrofluid with high stabilization. *Physica A: Stat. Mech. Appl.* **2015**, *438*, 560–567.
[39] Berger, P.; Adelman, N. B.; Beckman, K. J.; Campbell, D. J.; Ellis, A. B.; Lisensky, G. C. Preparation and properties of an aqueous ferrofluid. *J. Chem. Educ.* **1999**, *76*, 943.
[40] Li, J.; Liu, X. D.; Lin, Y. Q.; Bai, L.; Li, Q.; Chen, X. M.; Wang, A. R. Field modulation of light transmission through ferrofluid film. *Appl. Phys. Lett.* **2007**, *91*, 253108.
[41] Răcuciu, M.; Creangă, D.; Călugăru, G. Synthesis and rheological properties of an aqueous ferrofluid. *J. Optoelectron. Adv. Mater.* **2005**, *7*, 2859–2864.
[42] Arantes, F. R.; Odenbach, S. The magnetoviscous effect of micellar solutions doped with water based ferrofluids. *J. Magn. Magn. Mater.* **2015**, *390*, 91–95.
[43] Liu, H. Y.; Yan, Z. Q.; Chen, F. The perfluoropolyether oil based ferrofluid and its sealing-related properties. *J. Magn. Mater. Devices* **2020**, *51*, 50–54.
[44] Wang, F. Research on preparation and property of fluorocarbon-based magnetic fluid. Master Degree Thesis, Beijing Jiaotong University, Beijing, China, 2013.
[45] Kharat, P. B.; Chavan, A. R.; Humbe, A. V.; Jadhav, K. M. Evaluation

of thermoacoustics parameters of $CoFe_2O_4$-ethylene glycol nanofluid using ultrasonic velocity technique. *J. Mater. Sci.: Mater. Electron.* **2019**, *30*, 1175–1186.
[46] Wang, C. G. High performance aqueous proton batteries based on MoO_3 and MnO_2. Ph.D. Dissertation, Shandong University, Jinan, China, 2022.
[47] Goya, G. F.; Berquó, T. S.; Fonseca, F. C.; Morales, M. P. Static and dynamic magnetic properties of spherical magnetite nanoparticles. *J. Appl. Phys.* **2003**, *94*, 3520–3528.
[48] Yamaura, M.; Camilo, R. L.; Sampaio, L. C.; Macêdo, M. A.; Nakamura, M.; Toma, H. E. Preparation and characterization of (3-aminopropyl) triethoxysilane-coated magnetite nanoparticles. *J. Magn. Magn. Mater.* **2004**, *279*, 210–217.
[49] Meng, J. H.; Yang, G. Q.; Yan, L. M.; Wang, X. Y. Synthesis and characterization of magnetic nanometer pigment Fe_3O_4. *Dyes Pigm.* **2005**, *66*, 109–113.
[50] Jing, X. W.; Liu, Y. Q.; Xu, Y.; Kang, Z. Q.; Dai, S. S. A drag reducer: It's interaction with water, synthesis and performance evaluation. *Drill. Fluid Completion Fluid* **2021**, *38*, 127–132.
[51] Zhang, L. N.; Li, D. H.; Yao, W. S.; Yang, R. J. Molecular dynamics simulation of interaction between GAP grafted hydantoin and solid oxidizers in for GAP propellant. *J. Propul. Technol.* **2010**, *31*, 587–592.
[52] Jiang, H.; Yue, H.; Liu, Q. Molecular dynamics simulation of mechanical properties and surface interaction for NR/BR blends. *China Plast.* **2012**, *26*, 64–68.
[53] Wang, Z. L.; Yan, X. L.; Huang, X. Y.; Li, Y. Q.; Gao, R. Y.; Fu, Z. Y. Molecular dynamics simulation of the effect of CNT-COOH content on the mechanical properties of PUR matrix composites. *Eng. Plast. Appl.* **2024**, *52*, 61–68.
[54] Amani, M.; Amjad-Iranagh, S.; Golzar, K.; Sadeghi, G. M. M.; Modarress, H. Study of nanostructure characterizations and gas separation properties of poly(urethane-urea) s membranes by molecular dynamics simulation. *J. Membr. Sci.* **2014**, *462*, 28–41.
[55] Cheng, Y. H.; Li, D. C.; Dai, R. K. Experimental analysis of starting torque of perfluoro polyethers-based magnetic fluid seal. *J. Harbin Eng. Univ.* **2017**, *38*, 1316–1321.
[56] Chi, C. Q. The Physical Foundations and Applications of Ferromagnetic Fluids; Beihang University Press: Beijing, 2011.
[57] Li, L.; Li, D. C.; Wang, L.; Liang, Z. Q.; Zhang, Z. L. Stable silicone oil based ferrofluids with well low-temperature fluidity applied to magnetic fluid seal. *J. Magn. Magn. Mater.* **2023**, *584*, 171077.
[58] Bing, H.; Ma, W. Laboratory investigation of the freezing point of saline soil. *Cold Reg. Sci. Technol.* **2011**, *67*, 79–88.
[59] Zhang, M. Y.; Zhang, X. Y.; Lu, J. G.; Pei, W. S.; Wang, C. Analysis of volumetric unfrozen water contents in freezing soils. *Exp. Heat Transfer* **2019**, *32*, 426–438.
[60] Liu, Z. C. Freezing point of wet soil and its measurement. *J. China Univ. Min. Technol.* **1986**, *3*, 24–31.
[61] He, P. The characteristic of soil electrical resistance in the process of freezing and its application. *J. Glaciol. Geocryol.* **1990**, *12*, 365–370.
[62] Kozlowski, T. Some factors affecting supercooling and the equilibrium freezing point in soil-water systems. *Cold Reg. Sci. Technol.* **2009**, *59*, 25–33.
[63] Ma, T. T.; Wei, C. F.; Xia, X. L.; Chen, P. Experimental study of effect of NaCl solution on soil freezing characteristic. *Rock Soil Mech.* **2017**, *38*, 1919–1925.
[64] Lu, J. G.; Zhang, M. Y.; Zhang, X. Y.; Pei, W. S.; Bi, J. Experimental study on the freezing-thawing deformation of a silty clay. *Cold Reg. Sci. Technol.* **2018**, *151*, 19–27.
[65] Fu, X. C.; Shen, W. X.; Yao, T. Y.; Hou, W. H. Physical Chemistry; 5th ed. Higher Education Press: Beijing, 2005.
[66] Liu, Y. Q. Logical analysis of deduction of cryoscopic formula. *J. Weinan Teach. Coll.* **2001**, *16*, 22–24.